

Cite this: *CrystEngComm*, 2012, 14, 6565–6572

www.rsc.org/crystengcomm

PAPER

Hydrothermal synthesis of needle-like hyperbranched $\text{Ni}(\text{SO}_4)_{0.3}(\text{OH})_{1.4}$ bundles and their morphology-retentive decompositions to NiO for lithium storage†

Wei Wen,^a Jin-Ming Wu,^{*a} Lu-Lu Lai,^a Guo-Ping Ling^a and Min-Hua Cao^b

Received 11th July 2012, Accepted 18th July 2012

DOI: 10.1039/c2ce26127h

In this work, nickel basic sulfate ($\text{Ni}(\text{SO}_4)_{0.3}(\text{OH})_{1.4}$) with a unique morphology of needle-like hyperbranched bundle was fabricated on a large scale *via* a template-free hydrothermal reaction between nickel acetate and dextran sulfate. The gradual release of OH^- from hydrolysis of the acetate plays a key role in the formation of the nanoneedle bundles. With increasing amounts of the dextran sulfate, the hydrothermal precipitates changed from stacked nanoplates to nanoneedle bundles and then to aggregated nanowires. Based on the crystal lattice analysis, a growing mechanism of the various nanostructures is proposed. The nanoneedle bundle architecture can be maintained after a subsequent heat treatment in air at a high temperature of 750 °C, which is significantly higher than the upper limit for most of the reported $\text{Ni}(\text{SO}_4)_{0.3}(\text{OH})_{1.4}$ to preserve the original nanostructures. Thanks to the extremely high morphology stability, the $\text{Ni}(\text{SO}_4)_{0.3}(\text{OH})_{1.4}$ nanoneedle bundles can be decomposed thoroughly to NiO nanoneedle bundles with high crystallinity. When utilized as anode materials for Li-ion battery, the NiO nanoneedle bundles presented a very high initial discharge capacity; but just like most NiO nanostructures, the cyclic stability remains to be further improved.

1. Introduction

Owing to the unique and fascinating properties in various applications, one-dimensional (1D) nanostructural materials, such as nanowires, nanotubes, nanorods, and nanoneedles, have stimulated tremendous research interest.^{1–6} A remarkable advantage of 1D nanostructures over zero-dimensional nanoparticles is that the high aspect-ratio favors charge transport.^{7,8} Conventional synthetic strategies to achieve 1D nanostructures are template-assisted methods, which are usually expensive and demand subsequent steps to remove the templates or organic additives.⁹ It is thus of great interest to achieve 1D nanomaterials utilizing neither templates nor surfactants, which in general relies on a fine control over the growing rates of various facets of the crystals.¹⁰

As inspired from the photosynthesis of natural plants, hyperbranched metal oxides are supposed to improve further the light harvesting efficiency and the charge separation efficiency.^{11–15} Compared with other 1D nanostructures, nanoneedles provide additional merits such as excellent field emission

property.¹⁶ However, hyperbranched nanoneedle structure is rarely reported.

$\text{Ni}(\text{OH})_2$ is a common positive electrode material for various nickel-based rechargeable batteries¹⁷ and also a promising candidate for supercapacitors because of its high capacity and low cost.¹⁸ $\text{Ni}(\text{OH})_2$ possesses two polymorphs, that is, α - and β -phases.¹⁹ β - $\text{Ni}(\text{OH})_2$ contains no intercalated species. α - $\text{Ni}(\text{OH})_2$ is a kind of layer hydroxides, which serves as electrodes, catalysts, selective retainers of anions, topotactic incorporators of cations, and metal oxide precursors.^{20,21} It consists of stacked $\text{Ni}(\text{OH})_{2-x}$ layers intercalated with various anions or water molecules and can be formulated as $\text{Ni}(\text{OH})_{2-x}(\text{A}^{n-})_{x/n} \cdot y\text{H}_2\text{O}$, where A^{n-} stands for anions such as SO_4^{2-} , CO_3^{2-} , NO_3^- and Cl^- . Up to now, various α - $\text{Ni}(\text{OH})_2$ 1D nanostructures have been synthesized, owing to the close relationship between microstructures and properties. For example, $\text{Ni}(\text{OH})_{1.66}(\text{SO}_4^{2-})_{0.17} \cdot 0.29\text{H}_2\text{O}$ nanoribbons were synthesized *via* a hydrothermal treatment of amorphous α - $\text{Ni}(\text{OH})_2$ with a high concentration of NiSO_4 at 100 °C for 24 h.²² Recently, Sun *et al.* fabricated $\text{Ni}(\text{SO}_4)_{0.3}(\text{OH})_{1.4}$ nanowires by hydrothermal treatment of NiSO_4 and NaOH . The anions of OH^- and SO_4^{2-} were reported to affect the resultant morphology.²³ $\text{Ni}(\text{OH})_{1.4}(\text{SO}_4^{2-})_{0.3}$ nanobelts were also achieved through hydrothermal reactions of NiSO_4 and ammonia in an ethanol–water solution²⁴ or by hydrothermal treatments of NiSO_4 and NaOH in aqueous solution.²⁵

$\text{Ni}(\text{OH})_2$ nanoneedles are seldom observed. Only one report exists that $\text{Ni}(\text{OH})_{1.4}(\text{SO}_4^{2-})_{0.3}$ nanoneedles (NOT nanoneedle bundles as reported in the current investigation) can be obtained

^aState Key Laboratory of Silicon Materials, Key Laboratory of Advanced Materials and Applications for Batteries of Zhejiang Province and Department of Materials Science and Engineering, Zhejiang University, Hangzhou, 310027, P. R. China. E-mail: msewj@zju.edu.cn; Fax: +86-571-87953115; Tel: +86-571-87953115

^bKey Laboratory of Cluster Science, Ministry of Education of China and Department of Chemistry, Beijing Institute of Technology, Beijing, 100081, P. R. China

† Electronic Supplementary Information (ESI) available: other SEM, XRD and EDS results. See DOI: 10.1039/c2ce26127h

by a forced hydrolysis of aqueous solutions containing nickel nitrate, nickel sulfate, and sodium acetate.²⁶ However, the nanoneedles cannot be maintained in the subsequent heat treatment at 500 °C to obtain pure NiO.²⁶ It turns out to be very difficult to maintain the original 1D nanostructures of α -Ni(OH)₂ after a subsequent calcination to achieve phase pure NiO.^{24,26,27} Recently, Yang *et al.* fabricated Ni(SO₄)_{0.3}(OH)_{1.4}/C nanobelts with a coaxial core-shell structure by two-step hydrothermal treatments to improve the morphology stability of Ni(SO₄)_{0.3}(OH)_{1.4} up to 600 °C.²⁷ Compared with Ni(OH)₂, NiO has much wider applications in catalysis,²⁸ lithium ion batteries,²⁹ electrochromic,³⁰ supercapacitors,³¹ magnetic materials,³² and resistive memory switches.³³ There appears to be no reports on the direct synthesis of NiO nanoneedles. Therefore, it is of great importance to achieve an α -Ni(OH)₂ 1D nanostructure which guarantees a morphology-retentive decomposition to well-crystallized NiO upon a high-temperature calcination.

Herein, we report a template-free hydrothermal synthesis of needle-like hyperbranched bundles of Ni(SO₄)_{0.3}(OH)_{1.4} with a very high morphology stability for up to 750 °C. NiO nanoneedle bundles have been achieved by annealing the as-synthesized Ni(SO₄)_{0.3}(OH)_{1.4} products. To the best of our knowledge, this is the first report on the synthesis of this morphology of Ni(SO₄)_{0.3}(OH)_{1.4} and NiO. By controlling the species and concentrations of reactants, Ni(OH)₂ with various nanostructures of nanoneedle bundles, stacked nanoplates, nanowires, and hierarchical microspheres can be fabricated by the one-pot hydrothermal procedure without any templates or surfactants, which is suitable for scale-up productions. The electrochemical property of the NiO nanoneedle bundles was also investigated.

2. Experimental section

2.1 Synthesis

All reagents were of analytical grade and used as received without further purification. Unless specified in the text, the typical synthetic process to fabricate needle-like hyperbranched bundles of Ni(SO₄)_{0.3}(OH)_{1.4} is as follows. 4.0 mmol nickel acetate tetrahydrate [Ni(CH₃COO)₂·4H₂O] and 1.0 μmol dextran sulfate [(C₆H₇Na₃O₁₄S₃)_{*n*}, CAS# 9011-18-1, M.W. 500 000] were dissolved in 40 mL deionized water to obtain a clear green solution. The solution was transferred into a Teflon-lined stainless steel autoclave to fill up 80% of its total volume (50 mL). The autoclave was sealed and kept in an oven maintained at 180 °C for 12 h and then cooled naturally to room temperature. The obtained precipitates were filtered and washed repeatedly with deionized water and absolute alcohol to remove the impurity, and dried at 80 °C in air. In order to investigate the structural evolution during the subsequent thermal treatment, some products were heated at 450 °C for 3 h, 700 °C for 5 h, and 750 °C for 3 h, respectively.

2.2 Characterization

X-ray diffraction (XRD) measurements were conducted on a Rigaku D/max-3B diffractometer with Cu-K α radiation, operated at 40 kV, 100 mA (λ = 0.15406 nm). The powder morphology was observed using a field emission scanning electron microscope (FE-SEM, Hitachi S-4800, Tokyo, Japan)

equipped with an energy-dispersive X-ray analysis (EDS) system and a FEI-F20 transmission electron microscopy (TEM, FEI, USA) working at 200 kV. A STA-449F3 instrument (NETZSCH-Gerätebau GmbH, Germany) was used to carry out the thermogravimetric (TG) analysis of the as-synthesized sample in an air atmosphere at a heating rate of 10 K min⁻¹ from room temperature to 900 °C. Fourier transform infrared spectrum (FT-IR) was recorded with the KBr pellet technique in the range of 4000–400 cm⁻¹ on a NICOTCT infrared spectrophotometer. The content of C, H, and N elements in the sample was determined by elemental analysis (Flash EA 1112, ThermoFinnigan). The X-ray photoelectron spectra (XPS) characterizations were carried out on a PHI-5000C ESCA system (Perkin-Elmer, USA) with Al K α radiation ($h\nu$ = 1486.6 eV) working at 250 W and 14.0 kV. The base pressure of the analyzer chamber was *ca.* 5 × 10⁻⁸ Pa. The binding energy (BE) was calibrated by using the containment carbon (C 1s = 284.5 eV).

2.3 Lithium storage test

The NiO nanoneedle bundles utilized for the lithium storage tests were prepared by the hydrothermal reaction between nickel acetate tetrahydrate and dextran sulfate at 180 °C for 12 h followed by calcination in air at 750 °C for 3 h. The working electrodes were prepared by a slurry coating procedure. The slurry consisted of 85 wt.% NiO powders, 10 wt.% acetylene black and 5 wt.% polyvinylidene fluoride (PVDF) dissolved in *N*-methyl pyrrolidone (NMP), and was coated on a copper foil, which acted as a current collector. The film was pressed under a pressure of 10 MPa after drying at 120 °C for 12 h in vacuum. The cells were assembled in an argon-filled glove box using Li foil as a counter electrode and polypropylene (PP) film (Celgard 2300) as a separator. The electrolyte was 1 M LiPF₆ in a 50 : 50 (w/w) mixture of ethylene carbonate (EC) and diethyl carbonate (DEC). The charge–discharge tests were conducted on a LAND 2001A system at a current density of 100 mA g⁻¹ between 0.02 V and 3.0 V. The cyclic voltammetry (CV) measurement was performed on a CHI660D electrochemical workstation at a scanning speed of 0.1 mV s⁻¹ between 0.02 V and 3.0 V (vs. Li/Li⁺).

3. Results and discussion

3.1 Synthesis of Ni(SO₄)_{0.3}(OH)_{1.4} nanoneedle bundles

Fig. 1a shows the XRD pattern of the as-synthesized precipitates. All the diffraction peaks can be indexed to the monoclinic phase of Ni(SO₄)_{0.3}(OH)_{1.4} (JCPDS 41-1424) with cell parameters of a = 0.789 nm, b = 0.296 nm, c = 0.463 nm and β = 91°. There are no peaks for other types of nickel hydroxyl, suggesting a high purity of the product. The EDS spectrum shown in Fig. 1b further confirms that there are Ni, O, and S elements in the product. The C element and excess amounts of O element came from the carbon paste used for preparations of the SEM sample, and also trace carbon or organics remained in the sample. Fig. 1c shows the FT-IR spectrum of the as-synthesized powder. The broad band at 3455 cm⁻¹ originates from the stretch vibrational mode of the absorbed water. The sharp band at 3602 cm⁻¹ results from the O–H band stretching vibration.²³ The bands between 600 and 1200 cm⁻¹ can be attributed to SO₄²⁻ and

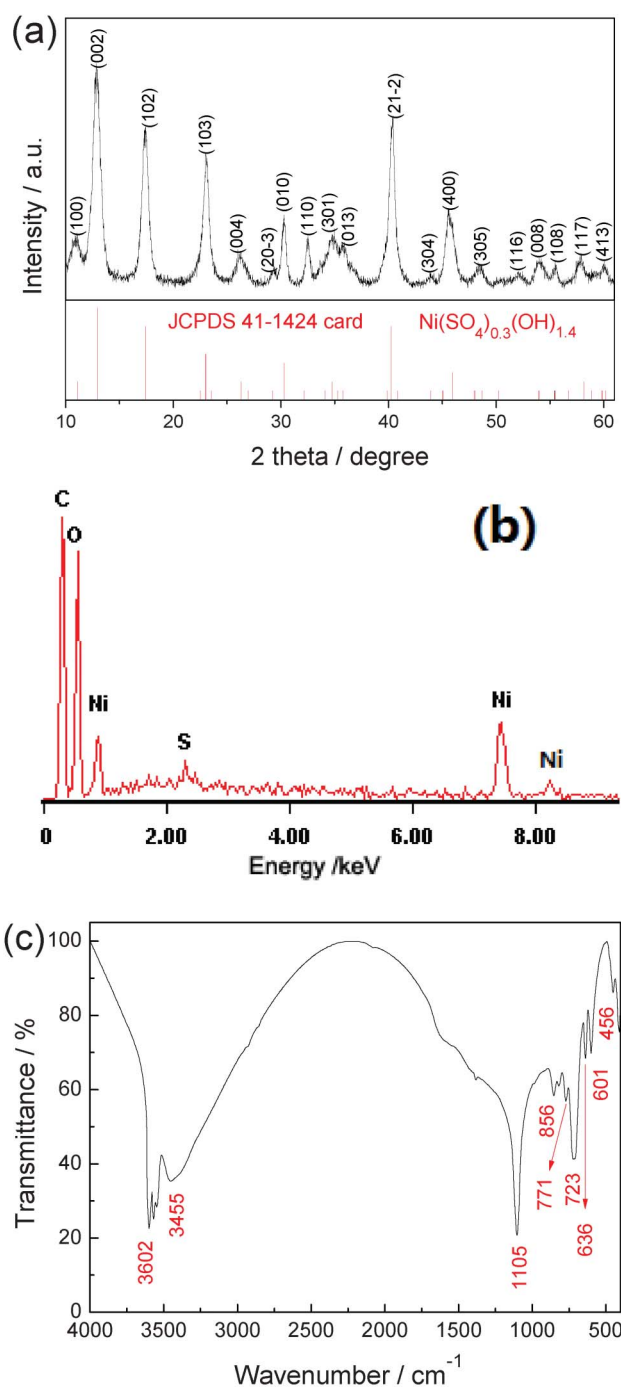


Fig. 1 XRD pattern (a), EDS spectrum (b), and FT-IR spectrum (c) of the as-synthesized $\text{Ni}(\text{SO}_4)_{0.3}(\text{OH})_{1.4}$.

HSO_4^- vibrations; within the band at 1105 cm^{-1} is attributed to the HSO_4^- vibrations.²⁷ Moreover, the band at 456 cm^{-1} is attributed to Ni–O vibrations. These results further confirm that the sample is the $\alpha\text{-Ni}(\text{OH})_2$ phase containing intercalated SO_4^{2-} .

The mass ratio of S to Ni is determined by XPS to be 0.169 (see Fig. S1 in the ESI†), which is consistent with the theoretical value of 0.164 for $\text{Ni}(\text{SO}_4)_{0.3}(\text{OH})_{1.4}$. The content of C and H elements in the sample is determined to be 4.6 wt.% and 2.4 wt.%, respectively, by elemental analysis, which detected no

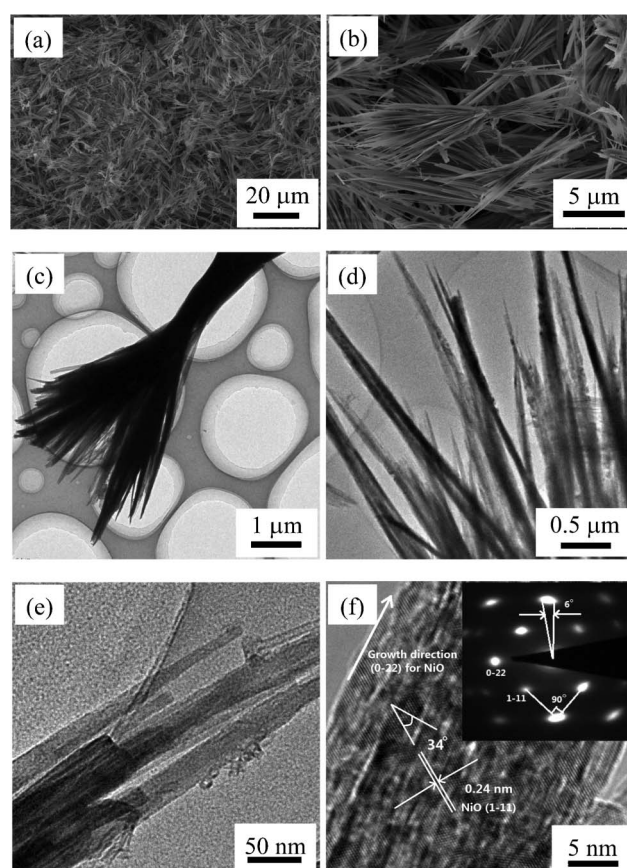


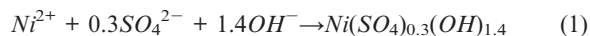
Fig. 2 SEM images (a, b), TEM images (c–e), and HRTEM image (f) of the as-synthesized $\text{Ni}(\text{SO}_4)_{0.3}(\text{OH})_{1.4}$. The inset in (f) shows the corresponding SAED pattern.

N element in the sample. The content of H element is higher than the theoretical value of 1.3 wt.% for $\text{Ni}(\text{SO}_4)_{0.3}(\text{OH})_{1.4}$. When more dextran sulfate (increase from 0.5 g to 0.6 g) was used to prepare the sample and an increased amount of C and H (5.7 wt.% C and 2.5 wt.% H) in the sample was obtained. Therefore, the main C element and the excess H result from some organics as a result of the incomplete decomposition of dextran sulfate.

Fig. 2a shows the representative SEM image of the as-synthesized $\text{Ni}(\text{SO}_4)_{0.3}(\text{OH})_{1.4}$ powders. It can be seen that the product exhibits needle-like hyperbranched bundle morphology with good uniformity and good dispersion in large quantity. A close observation (Fig. 2b) reveals that the bundles consist of many nanoneedles growing to diverse directions to form a sector-like cross section. The center parts of nanoneedles are adhered and fused together and their surfaces are smooth. The length of each nanoneedle is measured to be 7–10 μm . The TEM images (Fig. 2c, d) further exhibit that the product has a needle-like hyperbranched bundle structure. It is noted that some big nanoneedles consisted of several smaller ones adhering together (Fig. 2e), suggesting an oriented attachment mechanism for the formation of the large nanoneedles.^{25,34} The tip of an individual nanoneedle is measured to be less than 20 nm in diameter. Similarly to a previously reported $\text{Ni}(\text{SO}_4)_{0.3}(\text{OH})_{1.4}$,³⁵ the product is very sensitive to the electron-beam irradiation during TEM observations. The structure is destroyed in less than several

seconds under high-energy electron beam irradiations. Thus, it is difficult to obtain the HRTEM images and selected area electron diffraction (SAED) patterns of $\text{Ni}(\text{SO}_4)_{0.3}(\text{OH})_{1.4}$. As illustrated in Fig. 2f, the lattice fringes of $\text{Ni}(\text{SO}_4)_{0.3}(\text{OH})_{1.4}$ disappeared and plenty of nanoholes are observed. The spacing of 0.24 nm in Fig. 2f corresponds to the (1–11) planes of NiO. The SAED pattern (inset in Fig. 2f) further confirms that $\text{Ni}(\text{SO}_4)_{0.3}(\text{OH})_{1.4}$ thermally decomposed to NiO by electron irradiations under high vacuum conditions. It is worth mentioning that the NiO grains exhibit nearly the same orientation (Fig. 2f), and the tiny misorientation is *ca.* 6° (inset in Fig. 2f), which is slightly larger than that of nanobelts (namely, 3°).³⁵ Based on the geometrical relationship (angle in Fig. 2f), the growth direction of nanoneedles is determined to NiO [0–22]. The orientation relationship between $\text{Ni}(\text{SO}_4)_{0.3}(\text{OH})_{1.4}$ and NiO is [100]//[100], (020)//(022), and (008)//(0–22).³⁵ Thus, the growth direction of nanoneedles is $\text{Ni}(\text{SO}_4)_{0.3}(\text{OH})_{1.4}$ [008], that is, *z* axis of $\text{Ni}(\text{SO}_4)_{0.3}(\text{OH})_{1.4}$.

The main chemical reaction in the hydrothermal condition to obtain $\text{Ni}(\text{SO}_4)_{0.3}(\text{OH})_{1.4}$ nanoneedle bundles can be formulated as follows:



The SO_4^{2-} group is provided by the decomposition of dextran sulfate under hydrothermal conditions. Fig. 3a and 3b indicate that, $\text{Ni}(\text{SO}_4)_{0.3}(\text{OH})_{1.4}$ nanoneedle bundles can also be obtained by replacing dextran sulfate with Na_2SO_4 while maintaining the other conditions unchanged. Here, 4.0 mmol nickel acetate and 1.2 mmol Na_2SO_4 were used according to the stoichiometric ratio as illustrated in eqn (1).

The OH^- group comes from hydrolysis of the acetate, which means that Ni^{2+} cannot be precipitated in the absence of acetate. By substituting $\text{Ni}(\text{CH}_3\text{COO})_2$ with NiCl_2 , only uniform carbon microspheres can be obtained and no solid products containing Ni can be detected because of the absence of OH^- sources (Fig. 3c, d). The formation of the uniform carbon microspheres is attributed to the carbonization and polymerization of dextran sulfate in hydrothermal conditions, which is similar to those induced by dextran or glucose.

3.1.1 The effect of acetate on the formation of nanoneedle bundles

The gradual release of OH^- from hydrolysis of the acetate at elevated temperatures can slow down the reaction rate of Ni^{2+} with OH^- to control the nuclei formation and subsequent crystal growth, which is crucial for the synthesis of high-quality crystals.³⁶ In the current investigation, acetate plays an important role in the formation of nanoneedle bundles. A parallel experiment was carried out, in which $\text{Ni}(\text{CH}_3\text{COO})_2$ was replaced with NiCl_2 and urea, and dextran sulfate replaced with Na_2SO_4 . The amounts of Ni^{2+} and OH^- remained unchanged assuming a complete hydrolysis of anions. As illustrated in Fig. 3e, f, urchin-like microspheres consisting of nanowires were produced. Some broken microspheres suggest that they are hollow (circles in Fig. 3e). The product also contains some nanoneedles, as can be seen from the marked area in Fig. 3f. The XRD pattern suggests that the precipitates consisted of $\beta\text{-Ni}(\text{OH})_2$, together with a small amount of $\alpha\text{-Ni}(\text{OH})_2$ (see Fig. S2 in the ESI†). Considering the relative amounts of the

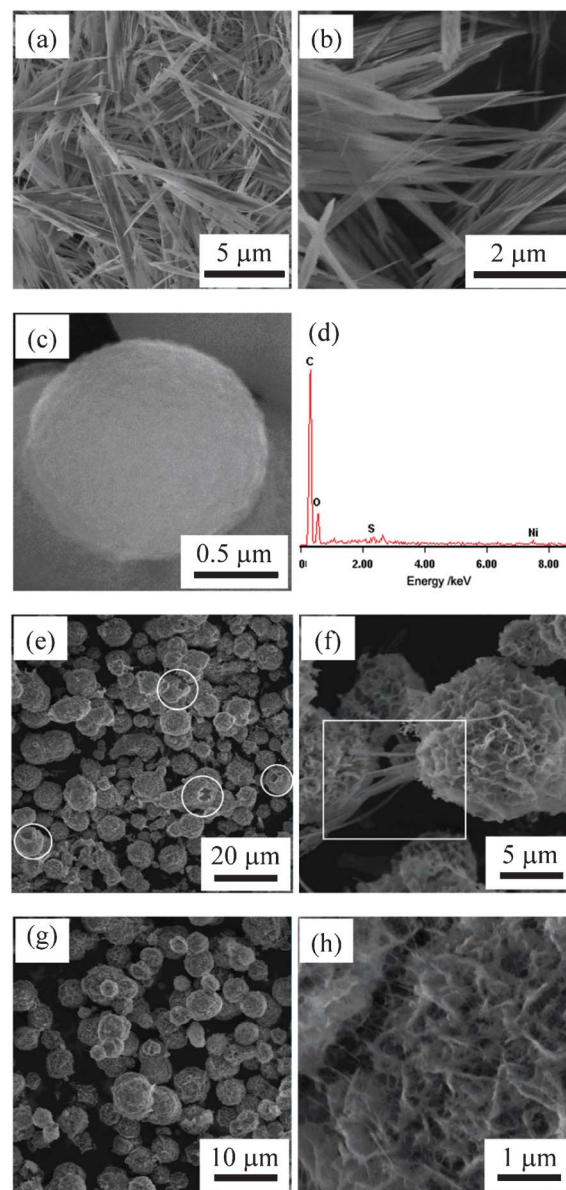


Fig. 3 (a, b) SEM images of the product derived from $\text{Ni}(\text{CH}_3\text{COO})_2 \cdot 4\text{H}_2\text{O}$ (4.0 mmol) and Na_2SO_4 (1.2 mmol). SEM image (c) and EDS spectrum (d) of the product derived from $\text{NiCl}_2 \cdot 6\text{H}_2\text{O}$ (4.0 mmol) and dextran sulfate (1 μmol). (e, f) SEM images of the product derived from $\text{NiCl}_2 \cdot 6\text{H}_2\text{O}$ (4.0 mmol), Na_2SO_4 (1.2 mmol), and urea (4.0 mmol). (g, h) SEM images of the product derived from $\text{NiCl}_2 \cdot 6\text{H}_2\text{O}$ (4.0 mmol) and urea (4.0 mmol).

microspheres and the nanoneedles, it can be assumed from the XRD pattern that the microspheres are $\beta\text{-Ni}(\text{OH})_2$ and the nanoneedles are $\text{Ni}(\text{SO}_4)_{0.3}(\text{OH})_{1.4}$. To support the assumption, Fig. 3g and 3h illustrates the SEM images of the precipitates collected from the hydrothermal reaction between NiCl_2 and urea. It can be seen that, only microspheres similar to those illustrated in Fig. 3e,f can be obtained when expelling Na_2SO_4 from the reactants. Hydrolysis of urea at temperatures higher than 85°C in aqueous solutions can gradually and homogeneously release OH^- ,³⁷ which has been used to synthesize three-dimensional hierarchical structures.³⁸

The two parallel experiments above-mentioned (Fig. 3e–h) suggest that, a high urea/ SO_4^{2-} ratio is in favor of the formation of $\beta\text{-Ni}(\text{OH})_2$ microspheres; otherwise the formation of $\text{Ni}(\text{SO}_4)_{0.3}(\text{OH})_{1.4}$ nanoneedles are favored. Thus, we guess that the proportion of microspheres in the mixed products should decrease with increasing Na_2SO_4 content in the hydrothermal system containing Na_2SO_4 , urea and NiCl_2 . As expected, the proportion of microspheres in the mixed products decreased sharply with increasing Na_2SO_4 from 1.2 mmol to 2.4 mmol (see Fig. S3 in the ESI,[†] compared with Fig. 3e).

3.1.2 The effect of dextran sulfate on the formation of nanoneedle bundles

The effect of dextran sulfate on the morphology of products was also investigated. In the series of experiments, the amount of nickel acetate remained unchanged as 4.0 mmol and that of dextran sulfate increased from 0 to 1.6 μmol . Assuming a total decomposition, 1.0 μmol dextran sulfate with a molecular weight of 500 000 can supply 3.2 mmol SO_4^{2-} and 4.0 mmol nickel acetate can supply 8.0 mmol OH^- ; therefore, the $\text{SO}_4^{2-}/\text{OH}^-$ molar ratio in the reaction system increased from 0 to 0.64. In the absence of dextran sulfate, stacked and circular nanoplates with uniform sizes were obtained (Fig. 4a). These nanoplates are crystalline $\beta\text{-Ni}(\text{OH})_2$ with hexagonal brucite-like structures, as can be discerned from the XRD pattern illustrated in Fig. S4 in the ESI.[†] By slightly increasing the dextran sulfate, some needle-like structures appeared (Fig. 4b). Further increasing the amount of dextran sulfate resulted in the formation of nanoneedle bundles (Fig. 4c). It is noted that nanoneedle bundles can be formed in the presence of dextran sulfate with a concentration varying from 0.4 μmol to 1.2 μmol . Agglomerated nanowires

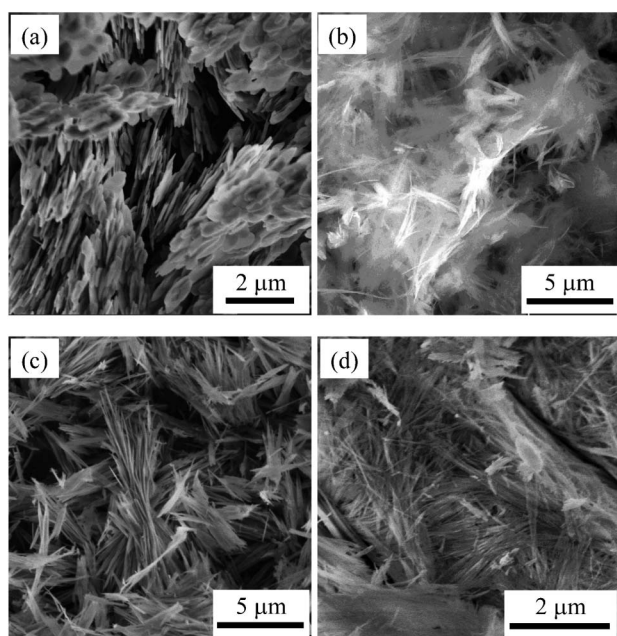


Fig. 4 SEM images of the products derived from hydrothermal reactions between nickel acetate tetrahydrate (4.0 mmol) and dextran sulfate with various amounts of (a) 0, (b) 0.2 μmol , (c) 1.2 μmol , and (d) 1.6 μmol .

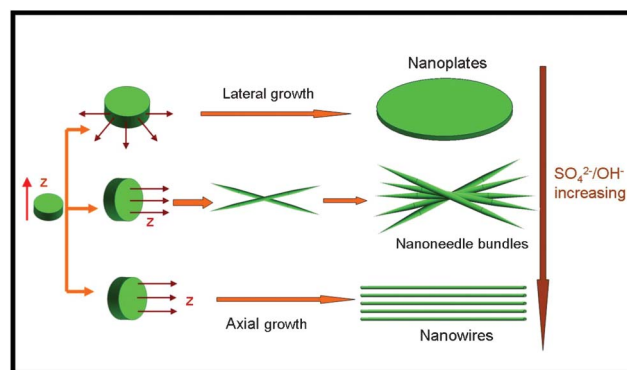


Fig. 5 Schematic image showing the formation of the $\text{Ni}(\text{OH})_2$ nanoplates and the $\text{Ni}(\text{SO}_4)_{0.3}(\text{OH})_{1.4}$ nanoneedle bundles and nanowires, with an increasing $\text{SO}_4^{2-}/\text{OH}^-$ ratio.

were obtained with a higher concentration of 1.6 μmol for dextran sulfate (Fig. 4d).

3.1.3 Crystal growth mechanism

To sum up, the effects of reaction conditions on the product morphology and a possible growth mechanism are represented in Fig. 5. $\alpha\text{-Ni}(\text{OH})_2$ and $\beta\text{-Ni}(\text{OH})_2$, the two polymorphs of nickel hydroxide, both crystallize in the hexagonal system by stacking $\text{Ni}(\text{OH})_2$ layers along the c axis. The difference arises when other anions are present between the stacking layers along the c axis. $\alpha\text{-Ni}(\text{OH})_2$ consists of stacked $\text{Ni}(\text{OH})_{2-x}$ layers intercalated in the interlayer space by various anions such as SO_4^{2-} . $\beta\text{-Ni}(\text{OH})_2$ has a brucite-like structure without any intercalated species and consisted of ABAB oxygen stacking sequence along the c axis.³⁹

In the absence of SO_4^{2-} , only $\beta\text{-Ni}(\text{OH})_2$ can be formed as a result of the reaction between Ni^{2+} and OH^- . $\beta\text{-Ni}(\text{OH})_2$ usually tends to form plate or sheet-like shapes, because it is a layered structure consisted of stacked units along the c axis. OH^- can selectively adsorb on certain crystal surfaces.²⁵ The quantity of OH^- adsorbed on (001) faces is much higher than those on other faces, such as (100), (010).^{23,40} Thus, $\beta\text{-Ni}(\text{OH})_2$ crystals grow rapidly along [100] and [010] directions to form plate-like shapes because of the large electrostatic repulsion of (001) planes.

The SO_4^{2-} ions can act as a capping agent in crystal growth. The steric hindrance effect of SO_4^{2-} ions determines the growth speed of different crystal planes and thus results in anisotropic crystal growth.²³ It is reported that the relative affinity of the layers toward different anions decreases in the following order: $\text{CO}_3^{2-} > \text{SO}_4^{2-} > \text{OH}^- > \text{F}^-$.⁴¹ Thus, SO_4^{2-} can intercalate into the interlayer spaces of $\text{Ni}(\text{OH})_2$ layers to form $\text{Ni}(\text{SO}_4)_{0.3}(\text{OH})_{1.4}$, and then 1D nanoneedles form owing to the stacking of the layers along the c axis, which is consistent with the TEM observation (Fig. 2f). The nanoneedles assemble together because of their interaction forces, and then thermally induced recrystallization may cause fusion on the central contacting point of each nanoneedle to minimize surface energy, leading to the formation of the present bundle-like nanoneedle structure. Further increasing the concentration of SO_4^{2-} is in favor of obtaining nanowires with a higher aspect ratio (see Fig. 4d), due to the rapid stacking and growing along the c axis.

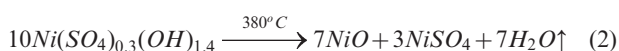
The formation of hierarchical microspheres in the urea-contained reactants may be attributed to the different rate of

OH^- releasing from the decomposition of urea and the hydrolysis of acetate, and also the different ability of urea and acetate to form metal complexes.⁴² The exact formation mechanism of the hierarchical microspheres is beyond the goal of the present study.

3.2 Morphology-retentive decomposition of $\text{Ni}(\text{SO}_4)_{0.3}(\text{OH})_{1.4}$ to NiO

In order to understand the thermal decomposition procedure, TG analyses of the as-synthesized $\text{Ni}(\text{SO}_4)_{0.3}(\text{OH})_{1.4}$ nanoneedle bundles (derived from 4.0 mmol nickel acetate and 1.0 μmol dextran sulfate) were carried out. As shown in Fig. 6, the thermal decomposition process can be divided into three stages according to the weight loss: Stage I, the loss of adsorbed water molecules from room temperature to 230 $^\circ\text{C}$; Stage II, the thermal decomposition of $\text{Ni}(\text{SO}_4)_{0.3}(\text{OH})_{1.4}$ and Stage III, the thermal decomposition of NiSO_4 . This thermal decomposition behavior agrees with that of $\text{Ni}(\text{SO}_4)_{0.3}(\text{OH})_{1.4}$ reported previously.^{24,26} The reactions in stage II and stage III can be formulated as follows²⁴:

Stage II:



Stage III:



Stage II in Fig. 6 shows that, the weight decreases from 97.1% to 75.6%, with a weight loss of *ca.* 21.5%, which is larger than that of 11.3% according to eqn (2). It suggests that the nanoneedles may contain some carbon or organics as a result of the incomplete decomposition of dextran sulfate, which is consistent with the elemental analysis result. In stage III, the weight decreases from 75.6% to 69.4%, with a weight loss of *ca.* 8.2%. This result is well consistent with the theoretical value of 8.1%, according to eqn (3).

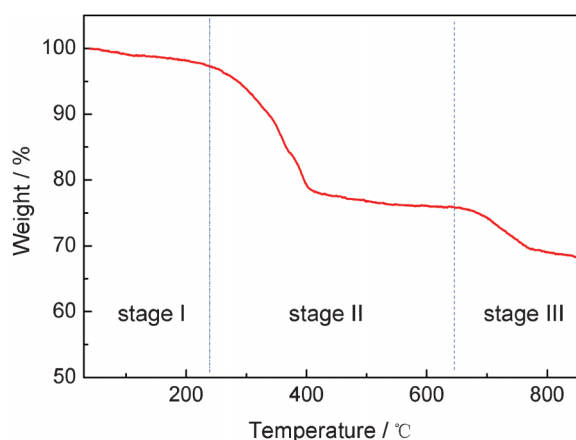


Fig. 6 TG curve of the as-synthesized $\text{Ni}(\text{SO}_4)_{0.3}(\text{OH})_{1.4}$ recorded under air atmosphere at a 10 K min^{-1} heating rate.

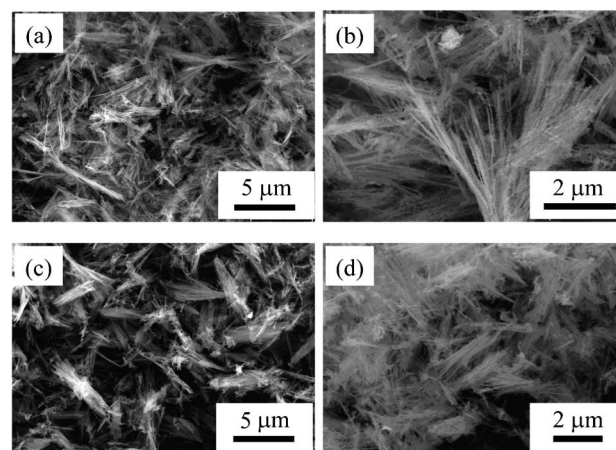


Fig. 7 SEM images of the $\text{Ni}(\text{SO}_4)_{0.3}(\text{OH})_{1.4}$ nanoneedle bundles annealed in air at 700 $^\circ\text{C}$ for 5 h (a, b) and 750 $^\circ\text{C}$ for 3 h (c, d).

The unique nanoneedle bundle morphology achieved in the current investigation can be well maintained even at high temperatures, such as 700 $^\circ\text{C}$ and 750 $^\circ\text{C}$ (Fig. 7), which is quite different from other $\text{Ni}(\text{SO}_4)_{0.3}(\text{OH})_{1.4}$ nanostructures.^{24,26} The XRD pattern in Fig. 8a illustrates that, after calcinations at 750 $^\circ\text{C}$ for 3 h in air, phase-pure and well-crystallized NiO can be obtained. The EDS spectrum (Fig. 8b) demonstrates that there is no S element in the calcined sample, further confirming the total decomposition of NiSO_4 . On the contrary, the sample annealed at 450 $^\circ\text{C}$ still contains plenty of S (see the EDS spectrum in Fig. S5 in the ESI†), which is well consistent with the TG results.

It is noted that the thermal decomposition of $\text{Ni}(\text{SO}_4)_{0.3}(\text{OH})_{1.4}$ nanoneedle bundles derived from nickel acetate and Na_2SO_4 (see Fig. 3a for the morphology of the as-synthesized product) at 750 $^\circ\text{C}$ for 3 h in air resulted in the collapse of the majority of nanoneedle bundles into nanoparticles (Fig. S6 in the ESI†). This is in good agreement with Ocaña, who reported that the $\text{Ni}(\text{OH})_{1.4}(\text{SO}_4^{2-})_{0.3}$ nanoneedles (NOT nanoneedle bundles as reported in the current investigation) fabricated through a forced hydrolysis of nickel nitrate, nickel sulfate and sodium acetate cannot be maintained in the subsequent heat treatment at 500 $^\circ\text{C}$.²⁶ Recently, Yang *et al.* improved the morphology stability of $\text{Ni}(\text{SO}_4)_{0.3}(\text{OH})_{1.4}$ nanobelts up to 600 $^\circ\text{C}$ by coating carbon shell from carbonization and polymerization of glucose.²⁷ It is argued here that dextran sulfate functions similarly to dextran or glucose in the hydrothermal environment, which contributes to the extremely high morphology stability upon

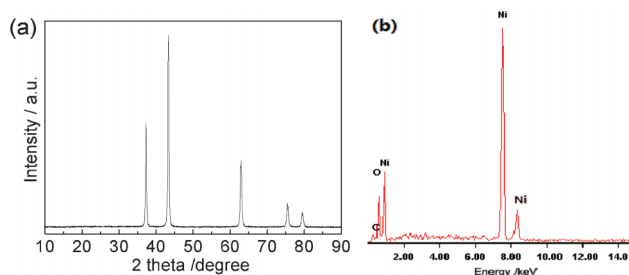


Fig. 8 XRD pattern (a) and EDS spectrum (b) of the $\text{Ni}(\text{SO}_4)_{0.3}(\text{OH})_{1.4}$ nanoneedle bundles annealed at 750 $^\circ\text{C}$ for 3 h in air.

calcination of the $\text{Ni}(\text{SO}_4)_{0.3}(\text{OH})_{1.4}$ nanoneedle bundles derived from nickel acetate and dextran sulfate. In contrast to the green color of $\text{Ni}(\text{SO}_4)_{0.3}(\text{OH})_{1.4}$ nanoneedle bundles derived from nickel acetate and Na_2SO_4 , the color of $\text{Ni}(\text{SO}_4)_{0.3}(\text{OH})_{1.4}$ nanoneedle bundles derived from nickel acetate and dextran sulfate is gray. Such a difference in color suggests that there may be carbon coating in the latter. However, the possible carbon coating has not been observed at the present time (Fig. 2f). The exact reason for the extreme high morphology stability is still unclear, which demands more in-depth investigations.

3.3 Lithium storage of NiO nanoneedle bundles

NiO has been considered to be one of the candidate materials to construct negative electrodes for rechargeable lithium-ion batteries because of its high theoretical specific capacity (718 mA h g^{-1}), environmental friendliness, low cost and natural abundance.^{43,44} Considering its morphology-dependent electrochemical properties and the unique morphology of NiO presented here, the electrochemical performance of the NiO nanoneedle bundles were evaluated by a standard NiO/Li coin type half cell, where NiO and Li foil serve as positive and negative electrodes, respectively. The cyclic voltammetry (CV) curves for the NiO nanoneedle bundles are shown in Fig. 9a. A strong peak at about 0.49 V and a weak peak at 1.34 V in the first cathodic scan is attributed to the initial reduction of NiO to Ni and the formation of amorphous Li_2O , associating the formation of the solid electrolyte interface (SEI).⁴⁵ There is a broad peak at about 2.32 V in the first anodic scan, corresponding to oxidation of Ni to NiO and decomposition of Li_2O to Li, and also an anodic peak at 1.46 V, corresponding to the partial decomposition of the polymeric coating on the NiO surface.^{45,46} The reaction mechanism of NiO with Li in lithium-ion batteries is proposed as follows in eqn (4):⁴⁷

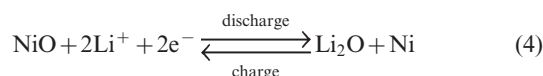


Fig. 9b demonstrates the first 3 charge–discharge voltage profiles of NiO nanoneedle bundles at a constant current of 100 mA g^{-1} . The discharge plateau at about 0.73 V in the first cycle is attributed to reduction of NiO to Ni, associating the formation of Li_2O , and the formation of the SEI.⁴⁸ The charge plateau at *ca.* 2.13 V represents oxidation of Ni to NiO, associating the reduction of LiO to Li, which is consistent with the CV results. In the first cycle, the discharge and charge capacity of NiO nanoneedle bundles is 2015 mA h g^{-1} and 1472 mA h g^{-1} . The irreversible capacity in the first cycle is assigned to the formation of the SEI layer and some undecomposed Li_2O phase, which is common for most anode materials. The NiO nanoneedle bundles exhibits a super-high discharge capacity of 1556 mA h g^{-1} in the second cycle, which is much larger than 925 mA h g^{-1} of commercial NiO nanoparticles (30 nm in size) and also larger than a high value of *ca.* 1200 mA h g^{-1} for NiO microspheres reported previously.⁴⁹ However, the cyclic stability is poor, and the discharge capacity decreases in the subsequent cycles (as shown in Fig. 9c), which is similar to that of many other NiO nanostructures reported.^{49–51} After 20 cycles, the

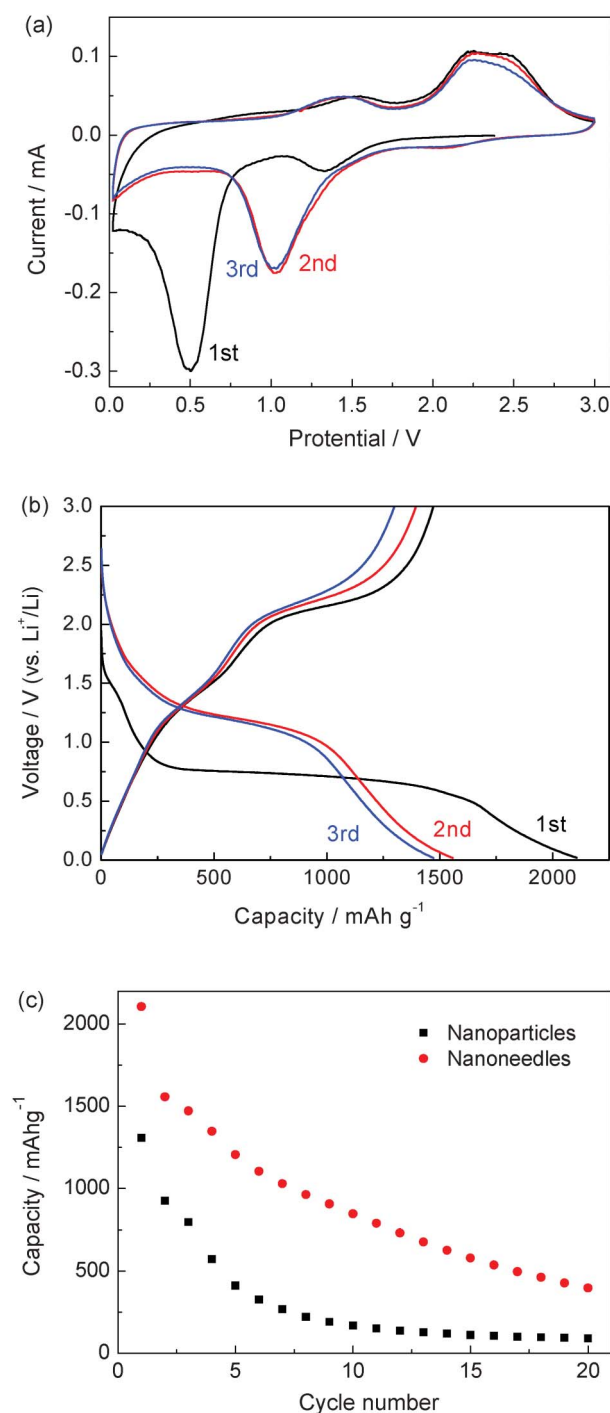


Fig. 9 (a) The first 3 cycles of cyclic voltammetry (CV) curves of NiO nanoneedle bundles. (b) Galvanostatic charge/discharge curves of NiO nanoneedle bundles at a current density of 100 mA g^{-1} (0.14 C). (c) Cycling performance of NiO nanoneedle bundles and nanoparticles (30 nm in size) at a current density of 100 mA g^{-1} .

discharge capacity of NiO nanoneedle bundles decreases to 397 mA h g^{-1} ; however, it is still much larger than that of NiO nanoflowers⁵⁰ and NiO nanorods.⁵¹ The discharge capacity of NiO nanoparticles is only 90 mA h g^{-1} at the 20th cycle. It is noted that the capacity of nanosheet-based NiO microspheres decreased sharply to a negligible level after 8 cycles even at a

lower current density of 50 mA g⁻¹.⁴⁹ The poor cyclic stability may be attributed to the secondary reactions involving electrolyte decomposition between the electrode and electrolyte.^{50,52} For practical use, the cyclability should be further improved via surface modification, for example, composites with carbon materials.^{53,54}

4. Conclusions

The hydrothermal reaction between nickel acetate and dextran sulfate at 180 °C for 12 h leads to the needle-like hyperbranched bundles of Ni(SO₄)_{0.3}(OH)_{1.4}. The nanoneedle bundle architecture can be maintained after a subsequent heat treatment in air at a high temperature of 750 °C, which makes it possible to achieve NiO nanoneedle bundles with high crystallinity. The two reactants of nickel acetate and dextran sulfate are found to be the key for the fabrication of the present nanoneedle bundles with extremely high morphology stability. The gradual release of OH⁻ from hydrolysis of the acetate favors the formation of the nanoneedle bundles. With increasing amounts of dextran sulfate, the resultant precipitates changed from stacked nanoplates to nanoneedle bundles and then to aggregated nanowires. The Ni(SO₄)_{0.3}(OH)_{1.4} nanoneedle bundles can also be achieved by a hydrothermal reaction between nickel acetate and Na₂SO₄; however, the morphology stability is poorer than that achieved by the hydrothermal reaction between nickel acetate and dextran sulfate. When utilized as anode materials for Li-ion batteries, the NiO nanoneedle bundles possessed a very high initial discharge capacity; however, the cyclic stability remains to be further improved.

References

- 1 J. Y. Tang, Z. Y. Huo, S. Brittman, H. W. Gao and P. D. Yang, *Nat. Nanotechnol.*, 2011, **6**, 568.
- 2 J. Joo, B. Y. Chow, M. Prakash, E. S. Boyden and J. M. Jacobson, *Nat. Mater.*, 2011, **10**, 596.
- 3 P. Roy, S. Berger and P. Schmuki, *Angew. Chem., Int. Ed.*, 2011, **50**, 2904.
- 4 R. H. Tao, J. M. Wu, H. X. Xue, X. M. Song, X. Pan, X. Q. Fang, X. D. Fang and S. Y. Dai, *J. Power Sources*, 2010, **195**, 2989.
- 5 B. Ludi, M. J. Süess, I. A. Werner and M. Niederberger, *Nanoscale*, 2012, **4**, 1982.
- 6 X. W. Lou, D. Deng, J. Y. Lee, J. Feng and L. A. Archer, *Adv. Mater.*, 2008, **20**, 258.
- 7 X. Yang, A. Wolcott, G. Wang, A. Sobo, R. C. Fitzmorris, F. Qian, J. Z. Zhang and Y. Li, *Nano Lett.*, 2009, **9**, 2331.
- 8 X. M. Song, J. M. Wu and M. Yan, *Electrochem. Commun.*, 2009, **11**, 2203.
- 9 F. Tian, J. Zhu and D. Wei, *J. Phys. Chem. C*, 2007, **111**, 12669.
- 10 Y. Feng, M. Zhang, M. Guo and X. Wang, *Cryst. Growth Des.*, 2010, **10**, 1500.
- 11 J. M. Wu and B. Qi, *J. Phys. Chem. C*, 2007, **111**, 666.
- 12 M. J. Bierman and S. Jin, *Energy Environ. Sci.*, 2009, **2**, 1050.
- 13 L. Y. Pan, Y. L. Zhang, H. Y. Wang, H. Liu, J. S. Luo, H. Xia, L. Zhao, Q. D. Chen, S. P. Xu, B. R. Gao, L. M. Fu and H. B. Sun, *Nanoscale*, 2011, **3**, 2882.
- 14 Y. Qiu, K. Yan, H. Deng and S. Yang, *Nano Lett.*, 2012, **12**, 407.
- 15 S. H. Ko, D. Lee, H. W. Kang, K. H. Nam, J. Y. Yeo, S. J. Hong, C. P. Grigoropoulos and H. J. Sung, *Nano Lett.*, 2011, **11**, 666.
- 16 R. C. Wang and C. H. Li, *Cryst. Growth Des.*, 2009, **9**, 2229.
- 17 D. Linden, *Handbook of Batteries*, 3rd ed. MxGraw-Hill, New York, 2002.
- 18 H. L. Wang, H. S. Casalongue, Y. Y. Liang and H. J. Dai, *J. Am. Chem. Soc.*, 2010, **132**, 7472.
- 19 B. H. Liu, S. H. Yu, S. F. Chen and C. Y. Wu, *J. Phys. Chem. B*, 2006, **110**, 4039.
- 20 G. G. C. Arizaga, K. G. Satyanarayana and F. Wypych, *Solid State Ionics*, 2007, **178**, 1143.
- 21 M. Meyn, K. Beneke and G. Lagaly, *Inorg. Chem.*, 1993, **32**, 1209.
- 22 D. Yang, R. Wang, J. Zhang and Z. Liu, *J. Phys. Chem. B*, 2004, **108**, 207531.
- 23 D. Sun, J. Zhang, H. Ren, Z. Cui and D. Sun, *J. Phys. Chem. C*, 2010, **114**, 12110.
- 24 Y. Tang, Z. Jia, Y. Jiang, L. Li and J. Wang, *Nanotechnology*, 2006, **17**, 5686.
- 25 L. Dong, Y. Chu and W. Sun, *Chem.-Eur. J.*, 2008, **14**, 5064.
- 26 M. Ocaña, *J. Colloid Interface Sci.*, 2000, **228**, 259.
- 27 D. Yang, P. Liu, Y. Gao, H. Wu, Y. Cao, Q. Xiao and H. Li, *J. Mater. Chem.*, 2012, **22**, 7224.
- 28 J. C. Hu, K. K. Zhu, L. F. Chen, H. J. Yang, Z. Li, A. Suchopar and R. Richards, *Adv. Mater.*, 2008, **20**, 267.
- 29 H. Liu, G. X. Wang, J. Liu, S. Z. Qiao and H. Ahn, *J. Mater. Chem.*, 2011, **21**, 3046.
- 30 M. C. A. Fantini, F. F. Ferreira and A. Gorenstein, *Solid State Ionics*, 2002, **152–153**, 867.
- 31 S. K. Meher, P. Justin and G. R. Rao, *Nanoscale*, 2011, **3**, 683.
- 32 F. Jiao, A. H. Hill, A. Harrison, A. Berko, A. V. Chadwick and P. G. Bruce, *J. Am. Chem. Soc.*, 2008, **130**, 5262.
- 33 R. Waser and M. Aono, *Nat. Mater.*, 2007, **6**, 833.
- 34 J. M. Wu and B. Qi, *J. Am. Ceram. Soc.*, 2008, **91**, 3961.
- 35 K. Zhang, J. Wang, X. Lu, L. Li, Y. Tang and Z. Jia, *J. Phys. Chem. C*, 2009, **113**, 142.
- 36 N. R. Jana, L. Gearheart and C. J. Murphy, *Adv. Mater.*, 2001, **13**, 1389.
- 37 M. Z. C. Hu, M. T. Harris and C. H. Byers, *J. Colloid Interface Sci.*, 1998, **198**, 87.
- 38 Z. Sun, J. H. Kim, Y. Zhao, F. Bijarbooneh, V. Malgras, Y. Lee, Y. M. Kang and S. X. Dou, *J. Am. Chem. Soc.*, 2011, **133**, 19314.
- 39 L. Xu, Y. S. Ding, C. H. Chen, L. Zhao, C. Rinkus, R. Joesten and S. L. Suib, *Chem. Mater.*, 2008, **20**, 308.
- 40 H. L. Xu, W. Z. Wang and W. Zhu, *Mater. Lett.*, 2006, **60**, 2203.
- 41 H. Li and J. Ma, *Chem. Mater.*, 2006, **18**, 4405.
- 42 E. Ocaña, *Colloid Polym. Sci.*, 1985, **15**, 483.
- 43 J. Cabana, L. Monconduit, D. Larcher and M. R. Palacin, *Adv. Mater.*, 2010, **22**, E170.
- 44 W. Wen and J. M. Wu, *ACS Appl. Mater. Interfaces*, 2011, **3**, 4112.
- 45 Y. J. Mai, J. P. Tu, X. H. Xia, C. D. Gu and X. L. Wang, *J. Power Sources*, 2011, **196**, 6388.
- 46 X. H. Huang, J. P. Tu, X. H. Xia, X. L. Wang, J. Y. Xiang and L. Zhang, *J. Power Sources*, 2010, **195**, 1207.
- 47 P. Poizot, S. Laruelle, S. Grugeon, L. Dupont and J. M. Tarascon, *Nature*, 2000, **407**, 496.
- 48 H. Liu, G. X. Wang, J. Liu, S. Z. Qiao and H. Ahn, *J. Mater. Chem.*, 2011, **21**, 3046.
- 49 L. Liu, Y. Li, S. Yuan, M. Ge, M. Ren, C. Sun and Z. Zhou, *J. Phys. Chem. C*, 2010, **114**, 251.
- 50 F. Cao, F. Zhang, R. Deng, W. Hu, D. Liu, S. Song and H. Zhang, *CrystEngComm*, 2011, **13**, 4903.
- 51 T. Kavitha and H. Yuvaraj, *J. Mater. Chem.*, 2011, **21**, 15686.
- 52 B. Zhang, X. C. Ye, C. M. Wang and Y. Xie, *J. Mater. Chem.*, 2007, **17**, 2706.
- 53 J. S. Chen, Z. Wang, X. C. Dong, P. Chen and X. W. Lou, *Nanoscale*, 2011, **3**, 2158.
- 54 Y. Zou and Y. Wang, *Nanoscale*, 2011, **3**, 2615.